JOURNAL OF SOLID STATE CHEMISTRY 59, 332–347 (1985)

# Compounds of Molybdenum and Tungsten with High Specific Surface Area

## I. Nitrides

LEO VOLPE AND M. BOUDART[1]

*Department of Chemical Engineering, Stanford University, Stanford, California 94305*

Received November 5, 1984

Temperature-programmed reaction between $MoO_3$ or $WO_3$ with $NH_3$ provides a new way to prepare $Mo_2N$ and $W_2N$ powders with specific surface areas as high as 220 and 91 $m^2 g^{-1}$, respectively, corresponding to 3- to 4-nm crystallites. The transformation of $MoO_3$ platelets is topotactic in the sense that {100} planes of $Mo_2N$ are parallel to {010} planes of $MoO_3$. As the $MoO_3$ reacts with $NH_3$, it passes through an oxynitride intermediate with changing bulk structure, increasing surface area, and decreasing oxidation state of the metal. The product consists of highly porous nitride platelets, pseudomorphous with the original $MoO_3$. 

## Introduction

Synthetic solid-state chemistry aims at producing well-defined and reproducible materials. In this work, the solids of interest consist of molybdenum and tungsten nitride powders with useful properties. The nitride of molybdenum is one of the less-explored transition-metal nitrides, and next to nothing is known about the nitride of tungsten. The most familiar phases, $\gamma$-$Mo_2N$ and $\beta$-$W_2N$, are refractory metallic solids with mechanical and thermal properties suitable for cutting tools, wear-resistant parts, and high-temperature structural applications. Molybdenum nitride is extremely hard (*1–3*). As electronic conductors, the nitrides possess attractive electrical and magnetic properties. For instance, thin-film resistors of $W_2N$–W and $Mo_2N$–Mo exhibit high resistivities and low temperature coefficients of resistance (*4*). Also, in contrast to pure molybdenum and tungsten, which are poor superconductors, the nitrides are known to have high superconducting transition temperatures (*5*). A theoretical estimate predicts this value to be close to 30 K for a hypothetical MoN (*6*).

One of the potential applications of $Mo_2N$ and $W_2N$ powders is in heterogeneous catalysis. The combination of Mo or W with N atoms on the surface may give rise to catalytic activity or selectivity similar to those reported for WC, a related material (*7*). Indeed, $\gamma$-$Mo_2N$ and $\beta$-$W_2N$ powders are among the active catalysts for $NH_3$ synthesis (*8*), while $Mo_2N$ is a catalyst for methane formation from $CO_2$ and CO (*9*), ethylene hydrogenation at 195 K, $H_2$–$D_2$ equilibration at 78 K (*10*), and *ortho–para* hydrogen conversion (*11*).

To use the nitrides efficiently in catalysis, their powders must be prepared with high

[1] To whom queries should be addressed.

0022-4596/85 $3.00

specific surface area, $S_g$. The most common way to produce the nitrides involves a reaction between the parent metal and $NH_3$ or its mixtures at 873–1073 K (*12*), but products have low values of $S_g$ (1 $m^2$ $g^{-1}$). The $Mo_2N$ powder with the highest reported value of $S_g$ (50 $m^2$ $g^{-1}$) was synthesized by reduction of $MoO_3$ in $H_2$ to Mo metal at 773 K and subsequent nitridation with 1% $NH_3$ in $H_2$ at 803 K (*13*).

Reactions of the trioxides with $NH_3$ have been explored before. Kiessling and Peterson (*14*) found the product of the $WO_3/NH_3$ reaction at 973 K to consist of an oxide–nitride with a defective B1 (NaCl) structure. Lyutaya (*15*) studied the $MoO_3$ and $WO_3/NH_3$ reactions between 873 and 1173 K. Molybdenum trioxide was transformed at 873 K into a material with a composition $MoO_2NH_2$ and an unresolved crystal structure, and at higher temperatures into a mixture of a face-centered cubic (fcc) oxynitride and other oxides. With tungsten trioxide, a compound $WO_2NH_2$ with an unresolved structure was formed below 873 K and an oxynitride with an fcc crystal lattice at higher temperatures. Carpenter and Hallada (*16*) reported that $MoO_3$ was reduced to $MoO_2$ faster with $NH_3$ than with $H_2$.

We report here that in the $MoO_3/NH_3$ reaction, only a small fraction of the solid converts to $MoO_2$, while the rest takes a different topotactic route, as shown by bulk and surface characterization of the intermediates of the reaction. The case of $WO_3$ will be considered in much less detail.

## Experimental

Most molybdenum compounds were synthesized from an ultrahigh purity trioxide powder, $MoO_3$-JM (Johnson Matthey, Puratronic, 99.998%). A few experiments employed a powder produced by decomposition of recrystallized ammonium molybdate (*17*), $MoO_3$-AM. All tungsten compounds were prepared from ultrahigh purity $WO_3$ (Aldrich, Gold Label, 99.999%).

All powder materials were synthesized at atmospheric pressure by downflow of $NH_3$ (Matheson, Anhydrous) at a rate of 70–100 $\mu$mol $s^{-1}$ over packed beds of trioxide. A typical experiment employed 0.2 to 1 g of precursor. The powder bed was contained in a quartz cell on top of a coarse fritted disk. The cell was designed both as a flow reactor and an adsorption cell. Its entire volume could be isolated by stopcocks and removed from the gas-delivery system to conduct all experiments *in situ*, without exposure of its contents to air. The temperature of the reactor could be varied, in a furnace or a bath, and monitored with a thermocouple.

To measure gas adsorption, the isolated cell was transferred and attached to a highly precise volumetric adsorption system (*18*). Following evacuation of the cell to $10^{-4}$ Pa at 100–200 K below the sample preparation temperature, an equilibrium CO (Matheson, 99.995%) adsorption isotherm was measured at room temperature (RT). Then the cell was evacuated again to $10^{-4}$ Pa to remove weakly adsorbed gas at RT. Then a second RT isotherm was obtained. Finally, $N_2$ (Matheson, 99.998%) was adsorbed and desorbed at liquid-nitrogen ($LN_2$) temperature. After these experiments, all samples were passivated at RT with a flowing mixture of 1% $O_2$ in He (Matheson, custom made).

The bulk structure of the samples was investigated by standard powder X-ray diffraction (XRD). The average size $d_c$ of a coherently diffracting domain perpendicular to (*hkl*) planes was calculated from the Scherrer equation, $d_c = K\lambda/\beta_{hkl}\cos\theta$, where $\theta$ is the Bragg angle, $\lambda$ the X-ray wavelength, and $\beta_{hkl}$ the peak width at half-maximum, corrected for instrumental broadening (*19*). The constant K was taken to be unity.

For optical microscopy molybdenum trioxide crystals, $MoO_3$-VP, were grown from the vapor phase (*20*) by D. Elwell of the

Center for Materials Research at Stanford University. They were treated with $NH_3$ the same way as the powder samples, passivated, and studied with a Carl Zeiss Standard WL microscope.

Specimens for transmission electron microscopy (TEM) were prepared by reaction of ammonia with $MoO_3$-AM powder. Passivated samples were dispersed ultrasonically in ethanol and then deposited on a TEM grid that had been coated with a holey carbon film. A Hitachi 500H microscope was operated at 100 kV.

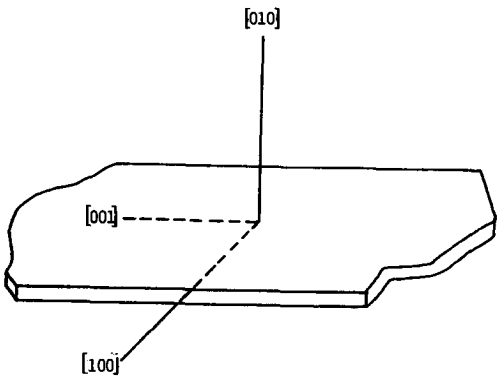


FIG. 2. Characteristic habit of $MoO_3$ crystals.

## Results and Discussion

### *Texture of the Reactants*

Molybdenum trioxide consists of layers of $MoO_6$ octahedra sharing corners and edges as shown in Fig. 1 (*21*). These $ReO_3$-type slabs are held together by van der Waals forces, lie in the (010) plane of the orthorhombic unit cell [space group *Pbmn* (*22*)], and lead to highly anisotropic platelets. Vapor-grown $MoO_3$ always forms platelets with extended (010) planes. The crystal cleaves preferentially along $(100)_{MoO_3}$, and as a result the platelet appears to have straight edges that are perpendicular to the [100] direction. Figure 2 portrays a typical platelet.

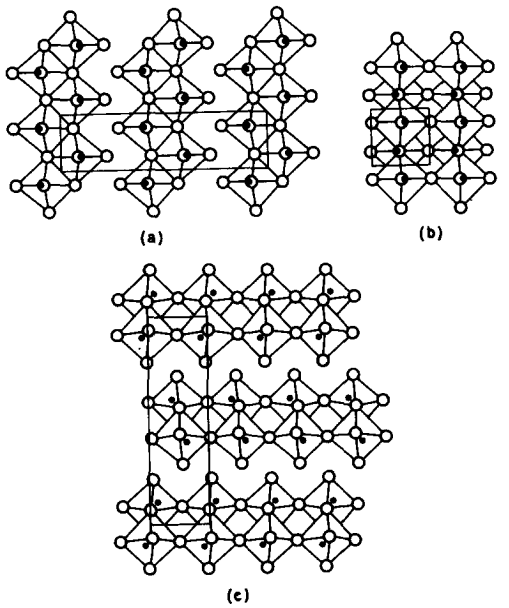


FIG. 1. Projections of the $MoO_3$ structure onto (a) (100), (b) (010), and (c) (001) planes, adapted with permission from Bursill (*21*). The unit cell is shown.

The $MoO_3$-JM powder consisted of transparent yellowish crystallites shaped as platelets, typically $50 \times 20 \times 0.3$ $\mu$m in the [001], [100], and [010] directions, respectively. This is illustrated by a scanning electron microscopy (SEM) picture in Fig. 3a. The powder exhibited a type III $N_2$ adsorption isotherm at $LN_2$ temperature (Fig. 4) (*23*), which is not, as a rule, amenable to the BET analysis because multilayer formation commences before the completion of the monolayer, as a result of very weak gas–solid interactions. Therefore, the formal $N_2$ BET $S_g$ of 0.8 $m^2 g^{-1}$ for this powder represents a rough estimate, corresponding to a platelet thickness of 0.53 $\mu$m, equal to $2/\rho S_g$ (*24*) where the density $\rho = 4.69$ g $cm^{-3}$ for $MoO_3$. Thus, there is fair agreement between the values of platelet thickness observed by SEM and deduced from $N_2$ physisorption.

The XRD pattern of $MoO_3$-JM strongly reflected the platelet habit with anomalously high integrated intensities of all the $(0k0)_{MoO_3}$ reflections (*25*). Interestingly, the platelet morphology could be easily de-

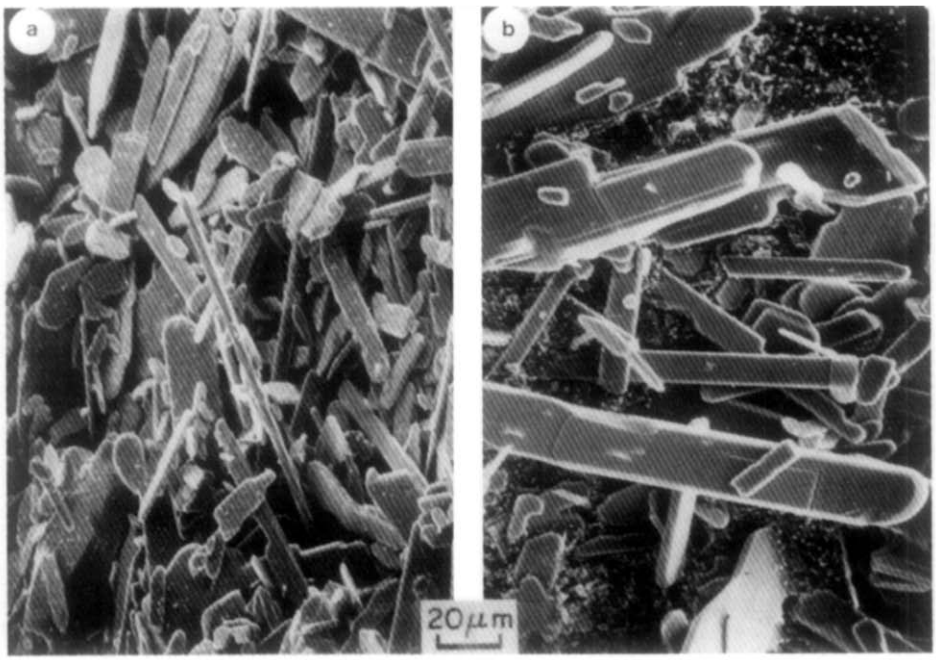


FIG. 3. Pseudomorphism in the reaction between $MoO_3$ and $NH_3$ revealed by scanning electron microscopy. (a) Parent $MoO_3$ powder (coated with Au–Pd). (b) Product $Mo_2N$ powder (supported on Ag paint).

stroyed by grinding in a mortar with a pestle. Relative peak intensities of the ground powder were identical to those tabulated in the Powder Diffraction File (*26*).

The $MoO_3$-AM sample consisted of thinner and less extended platelets, typically 20 × 10 × 0.1 μm in size (in the [001], [100], and [010] directions, respectively), as shown by SEM in Fig. 5. For this powder, too, the $N_2$ adsorption isotherm was of type III (Fig. 4), except at very low relative pressure. The formal BET $S_g$ was 13.2 $m^2\ g^{-2}$, corresponding to platelet thickness of 0.03 μm. The (0*k*0) XRD reflections of this sample had anomalously high relative intensities, which, again, reflected the platelet morphology, although the preferred orientation was not as pronounced as for $MoO_3$-JM.

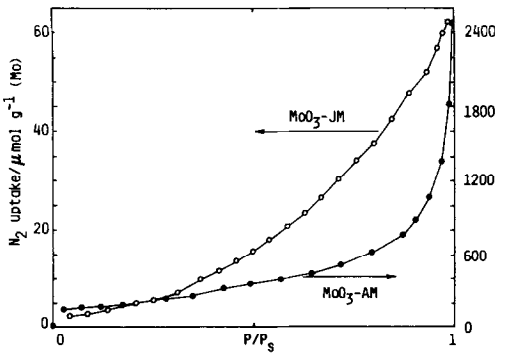


FIG. 4. Equilibrium $N_2$ adsorption isotherms for $MoO_3$-JM and $MoO_3$-AM powders obtained at $LN_2$ temperature. They have the uncommon type III shape.

Tungsten trioxide has a monoclinic (pseudo-orthorhombic) symmetry (space group $C_{2h}^5$-$P2_1/a$) (*27*). Its lattice expands with increasing temperature and at 593 K undergoes a phase transformation to orthorhombic with a higher symmetry (*28*). Like $MoO_3$, tungsten trioxide has a distorted $ReO_3$-type structure, but unlike its molybdenum counterpart, it has no well-defined layers. No platelet morphology is ex-

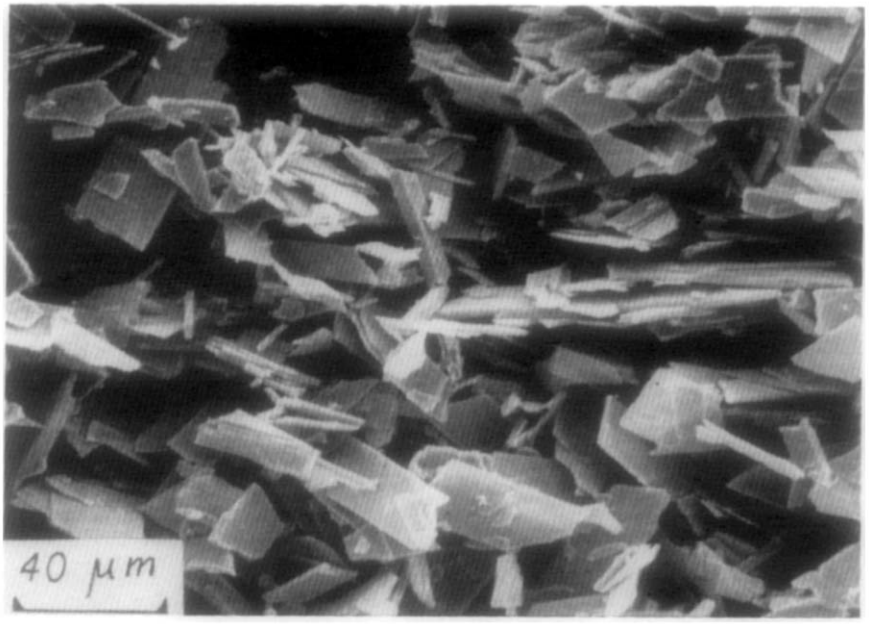


FIG. 5. Scanning electron micrograph of $MoO_3$-AM powder (coated with Pd–Au). The crystallites have a platelet morphology.

pected and none was found from the XRD pattern.

*Temperature-Programmed Reactions*

Syntheses of high-$S_g$ $Mo_2N$ and $W_2N$ were accomplished by temperature-programmed reactions, as shown in Fig. 6. Although the process conditions were not optimized, the temperature-time programs allowed considerable control over the rate and extent of transformation. The rate of temperature increase became important once the trioxides began to react at appreciable rates. This happened at around 630 and 700 K for $MoO_3$ and $WO_3$, respectively, as could be judged by darkening of the solid. Thereafter, the reaction, especially in its early stages, must be carried out slowly to avoid sintering. In the case of $MoO_3$, if the temperature was increased at a rate of 0.03 K $s^{-1}$ rather than 0.01 K $s^{-1}$ during the first linear heating interval (Fig. 6), the particles agglomerated to such a severe extent that they lost the properties of a fine powder. Excessively high temperatures used by previous investigators (*14*, *15*) to carry out the isothermal $MoO_3$, $WO_3/NH_3$ reactions could not yield high-$S_g$ nitrides. Our final temperatures of 980 and 1025 K were chosen to transform the powders to

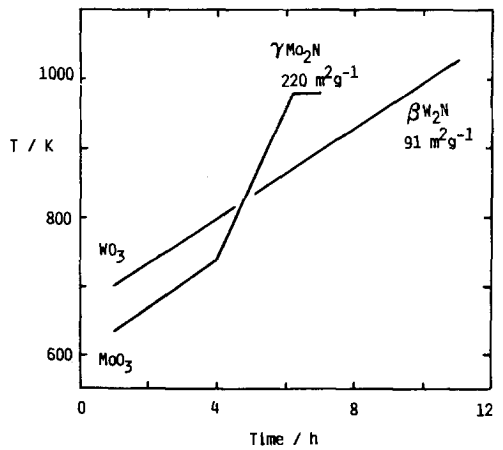


FIG. 6. Temperature-programmed nitride synthesis from $MoO_3$ and $WO_3$ powders in the presence of $NH_3$ at atmospheric pressure.

$Mo_2N$ and $W_2N$, respectively, within a few hours.

To minimize concentration gradients in the packed bed, a high ratio of $NH_3$ flow rate to the amount of powder had to be maintained. These gradients were caused both by formation of $H_2O$ vapor and by catalytic $NH_3$ decomposition at high temperature.

*Early Stages of Reaction*

Early stages of the $MoO_3/NH_3$ reaction were observed in a light-optical microscope by following the transparency loss of the large $MoO_3$-VP platelets. Some of them were as wide as 1 cm in the [100] direction and as long as several centimeters in the [001] direction.

A bright-field (BF) image of a part of one such platelet is shown by TEM in Fig. 7a. The corresponding selected-area diffraction pattern (SADP) is shown in Fig. 7b. The image has thickness fringes and bend extinction contours characteristic of almost perfect crystals. In the SADP, the $h + l$ even reflections give the brightest spots, and the $h + l$ odd ones are considerably less intense. Bursill (*21*) observed similar features in the TEM image and diffraction pattern of $MoO_3$ platelets. Noting that the $h + l$ odd reflections were prohibited by the $MoO_3$ symmetry, he attributed their presence to asymmetric excitation of the $(h0l)$ Laue zones.

When we treated $MoO_3$–VP platelets with $NH_3$ below 620 K, in exactly the same way we treated the powder samples, only slight darkening of gross $MoO_3$ crystal imperfections took place. Between 620 and 650 K, well-ordered straight ca. 2-$\mu$m-wide domains appeared and grew, as shown in Fig. 8a. The dark lines are oriented with respect to the $MoO_3$ crystal axes and form "herring bone" patterns. There are two kinds of domains: short and long ones. The short lines (ca. 50 $\mu$m) are spaced 5–10 $\mu$m apart. They form a $\pm 56.5°$ ($\pm 2°$) angle with $[100]_{MoO_3}$. The long ones extend up to several millimeters in the [001] direction.

A sequence of light-optical micrographs showed that during $NH_3$ treatment, patches of the short domains appeared on both the top and bottom of the platelet. They did not seem to originate from the platelet's edges or other visible defects. Also, an absence of any correspondence between the "herring bones" on the top and bottom faces, observed by focusing the microscope on either face, suggested that the domains did not extend deeply into the bulk in the [010] direction. With increase in the length of exposure to $NH_3$ and/or the temperature above 620 K, the short domains spread all over the platelet covering it rather uniformly. At the same time, the long, [001] domains started to form in the midst of the short ones rather than independently. Finally, after an hour-long exposure at 635 K, the "herring bones" became thicker, and perhaps deeper, and the platelet lost its transparency. Figure 8b illustrates these stages of the pattern evolution. Micrographs of slightly reacted $MoO_3$-JM platelets showed similar "herring bones."

Both types of domains in $MoO_3$ have been observed before under different circumstances and on a smaller scale by TEM. Glemser and Lutz (*29*) and König (*30*) were the first to see the short kind of domains upon heating $MoO_3$ by electron bombardment. The latter termed them "Fiederung" (feather patterns). Hashimoto (*31*) ascribed them to intermediate phases during the $MoO_3 \rightarrow MoO_2$ reduction. Pernoux and Borrelli (*32*) labeled them "lames de parquet" (floor planks) and interpreted them as slightly changed $MoO_3$ structures caused by oxygen removal. A detailed TEM study by Bursill (*21*) estimated the "cross-hatched" domains to have the $MoO_{2.9975}$ composition and a $7 \times 7$ $MoO_3$ disordered superlattice of oxygen vacancies. The domain boundaries were planar, parallel to [010]. The author related their formation to

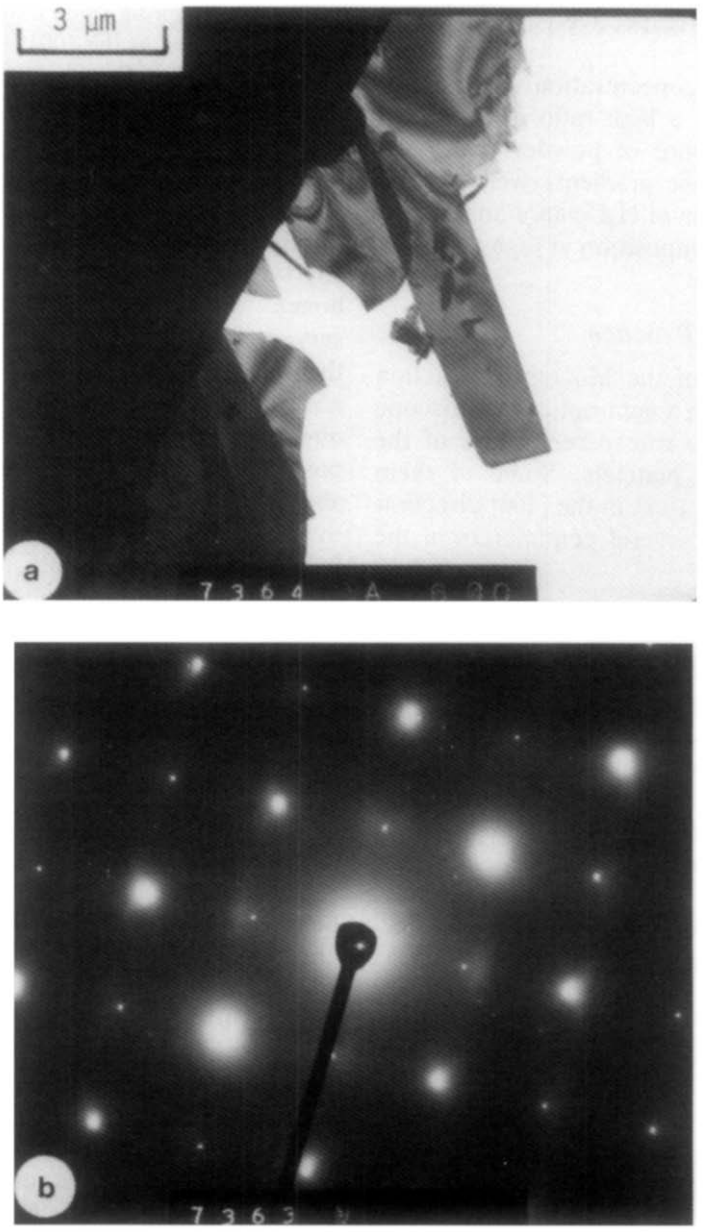


FIG. 7. Transmission electron microscopy of a $MoO_3$–VP platelet. (a) Bright-field image. (b) Diffraction pattern belonging to the $[010]_{MoO_3}$ zone axis. The $h + l$ even reflections give the brightest spots, and the $h + l$ odd ones are considerably less intense.

{120} crystallographic shear planes that displaced $MoO_3$ layers by $R = \pm a/2 + b/7$, where $a$ and $b$ are the vectors of the unit cell in the [100] and [010] directions, respectively. This shear is shown in Fig. 9.

Whereas other researchers reduced $MoO_3$ *in vacuo* and did not measure the transformation temperature, a TEM group at Oxford studied reduction by $H_2$ (partial pressure of 1 kPa) at temperatures up to 853

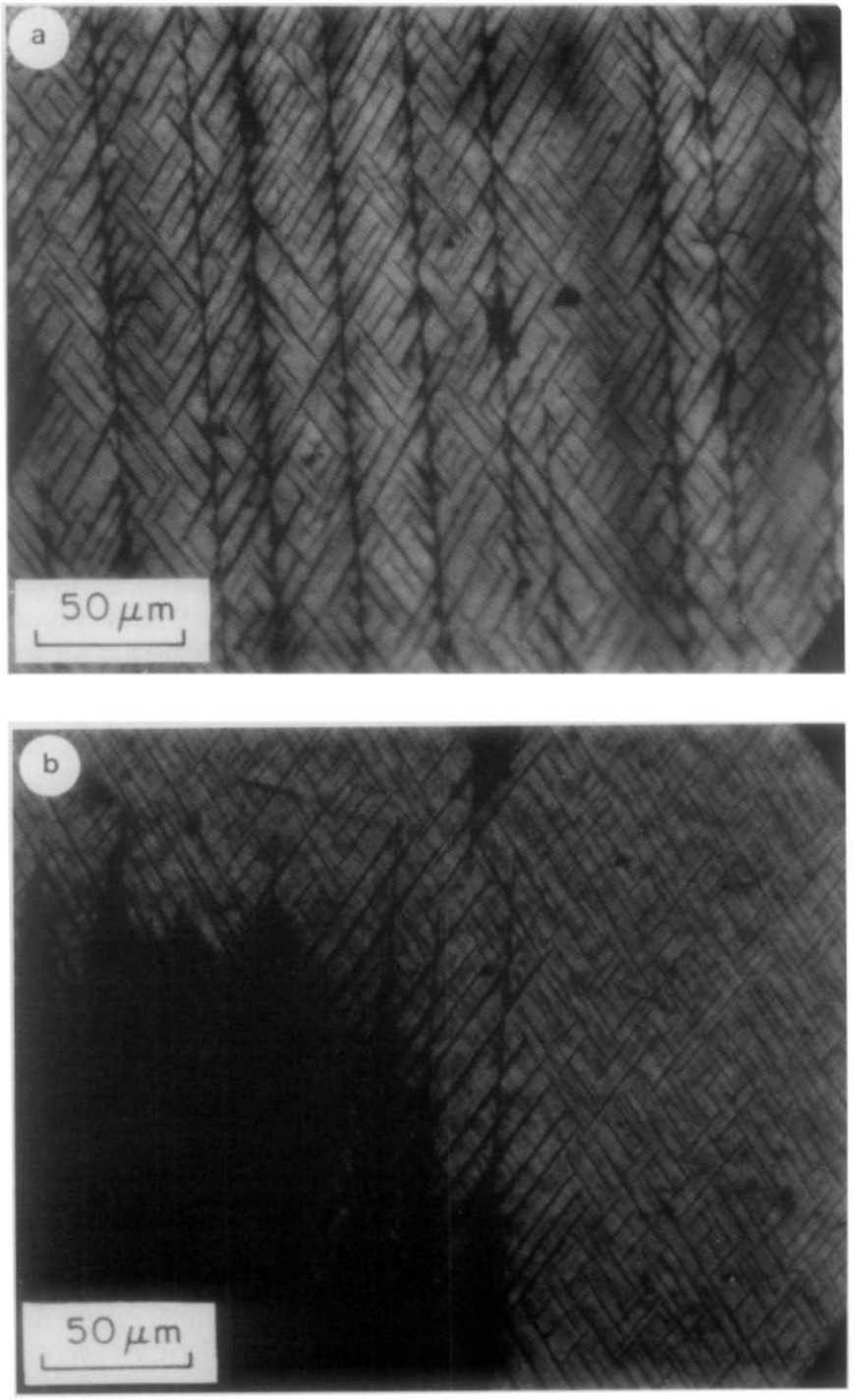


FIG. 8. Light-optical micrographs of $MoO_3$-VP platelets during early stages of the reaction with $NH_3$. (a) Crystallographically oriented domains of a reduced phase form "herring bone" patterns in the $MoO_3$ matrix. (b) Typical growth of the domains on the $(010)_{MoO_3}$ face.

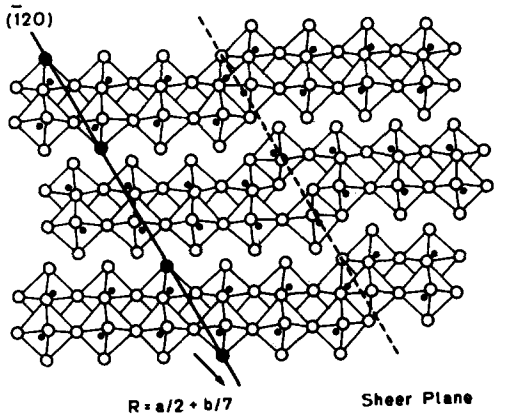


FIG. 9. Crystallographic shear during $MoO_3$ reduction proposed by Bursill (*21*). The marked oxygen vacancies preferentially collapse along (120) planes. The displacement vector is $R = a/2 + b/7$. In the process some $MoO_6$ octahedra go from corner to edge sharing. Adapted with permission from the author.

K (*33*). Note that the Pt heaters used in that work could dissociate $H_2$. In addition to Bursill's "cross-hatched" domains that grew in size with temperature up to 653 K, they observed at 673 K straight defects parallel to $[001]_{MoO_3}$ similar to our long lines in Fig. 8. They interpreted them as surface domains, ~30 nm deep, again related to crystallographic shear planes in $MoO_3$.

Although our "herring bones" are one to two orders of magnitude larger than those observed by TEM, they also form in the early stages of $MoO_3$ reduction, grow on the (010) faces, and are identically oriented. This suggests that the structure, composition, and formation mechanism of the domains is slightly reduced $MoO_3$ are independent of the reduction mode.

*Bulk Structure of Reaction Intermediates*

While $MoO_3$ reacted with $NH_3$ following the temperature program (Fig. 6), the solid morphology did not alter, viz., irrespective of the size and shape of the parent crystal, the products of the reaction turned out to be pseudomorphous with $MoO_3$. This is exemplified in Fig. 3 which shows side-by-side SEM pictures of $MoO_3$-JM crystals (Fig. 3a) and the product $Mo_2N$ platelets (Fig. 3b). Such morphology would ordinarily be uncharacteristic of $\gamma$-$Mo_2N$ where the metal atoms have an fcc arrangement, and the N atoms occupy every other octahedral interstitial site.

We interrupted the $MoO_3$, $WO_3/NH_3$ temperature programs (Fig. 6) at 638, 695, 770, 910, and 970 K and investigated the structure of passivated reaction intermediates by XRD. Owing to the platelet morphology in the $MoO_3$-JM case, comparison of XRD patterns of samples ground in a mortar with unground ones gave an opportunity to identify the planes parallel to the platelet (*25*).

When the $MoO_3$ structure collapsed above 660 K, it transformed to two phases: $MoO_2$ and one not previously described. No intermediate oxides such as substoichiometric Magnéli phases (*34*) could be detected. The new phase was an oxynitride as it contained Mo, O, and N. The amount of oxynitride substantially exceeded the $MoO_2$ fraction in the powders, judging from the relative diffraction intensities of the two phases.

On its way to $\gamma$-$Mo_2N$, the oxynitride structure changed. Below 700 K, the unground samples gave three equally intense XRD peaks corresponding to interplanar spacings 615, 307, and 205 pm. Between 700 and 770 K, the former two reflections lost intensity and disappeared, while the latter grew and shifted from 205 to 206 pm, and a small 103-pm peak appeared. Between 770 and 910 K the two remaining reflections of the oxynitride intensified, and their values of interplanar spacing increased further to 208 and 104 pm. As the temperature rose further to the final 980 K, these peaks remained unaltered, while reflections from other planes spaced 240, 147, and 126 pm apart developed. They corresponded to the (111), (220), and (311) planes of $\gamma$-$Mo_2N$ (*35*), and the earlier 208- and

104-pm lines, exceeding the rest in intensity by more than an order of magnitude, were those of (200) and (400) planes. Throughout this structural evolution, all coherently diffracting domains ranged from 5 to 7 nm. In the ground samples, on the other hand, the oxynitride planes were barely detectable, and the $(h00)_{Mo_2N}$ reflections had "normal" relative intensity. Hence the $\{100\}_{Mo_2N}$ planes were parallel or nearly parallel to the platelet (*25*).

The restacking of layers is schematically represented in Fig. 10. At first, the interplanar spacing is 615 pm, which can be viewed as an 11% contraction of the $MoO_3$ slabs with $b/2 = 692.5$ pm. Next, the symmetry changes so that the distance between equivalent layers is now 205 pm, and the planes $205 \times 3 = 615$ pm apart give a superlattice that disappears with rising temperature. The value of interlayer spacing is close to that of the crystallographic shear displacement of $b/7 = 198$ pm between the $(010)_{MoO_3}$ slabs (Fig. 9), but the agreement may be coincidental. Subsequently, the spacing increases to 208 pm—exactly the distance between the (200) $Mo_2N$ planes. Not until the high temperatures, where the rest of $\gamma$-$Mo_2N$ reflections appear, is there long-range order between Mo atoms within the layers.

In the final product, the $\{100\}_{Mo_2N}$ planes

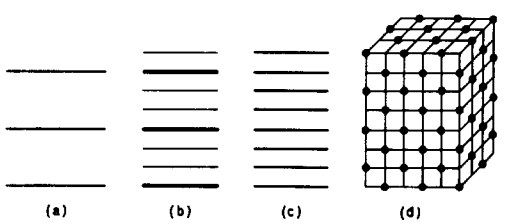


FIG. 10. Scheme of layer rearrangement in the oxynitride phase during the $MoO_3/NH_3$ reaction. (a) $(010)_{MoO_3}$ slabs spaced 692.5 pm apart. (b) Abrupt 11% contraction to 615 pm, following which the interlayer spacing becomes 205 pm with a $\times 3$ superlattice. (c) The spacing increases to 208 pm as the superlattice disappears. (d) The layers become $(200)_{Mo_2N}$ planes as the fcc structure evolves.

are parallel to the platelet. Hence, the process belongs to the class of topotactic reactions (*36*) because the solid product has a well-defined crystallographic orientation relative to the parent $MoO_3$. In particular, the {100} planes of $Mo_2N$ are parallel to the {010} layers of $MoO_3$, or $\{100\}_{Mo_2N}//\{010\}_{MoO_3}$.

We did not prepare the oxynitride phase separately. Molybdenum dioxide, appearing together with it, underwent no detectable structural changes during the oxynitride transformation. Only above 930 K did it react with $NH_3$ to convert, as the rest of the powder, to $Mo_2N$. The composition of the final product was very close to stoichiometric, according to elemental analysis. Since $MoO_2$ stayed in the form of large crystallites giving narrow XRD peaks, it hardly contributed to the tremendous increase in $S_g$ described in the next section. We found no orientation relationship between $MoO_3$ and $MoO_2$, although reduction of the trioxide to dioxide in $H_2$ was shown to be topotactic (*37*). When we treated $MoO_2$ powder (Alfa Products) with $NH_3$ exactly as we treated $MoO_3$, the product exhibited only the XRD peaks of the starting material. Therefore, $MoO_2$ plays merely a spectator role in the $MoO_3/NH_3$ reaction.

The fact that oxynitride peaks are broad and difficult to resolve, in ground samples, may explain why Carpenter and Hallada (*16*) did not report this phase after prolonged $NH_3$ treatment of $MoO_3$ at 620–670 K. In all likelihood, the "phase $x$" (with composition $MoO_2NH_2$ and unresolved crystal structure) observed by Lyutaya (*15*) along with $MoO_2$ during the $MoO_3/NH_3$ reaction was similar to our oxynitride.

### *Evolution of $S_g$ and Porosity*

Figure 11 shows equilibrium $N_2$ adsorption and desorption isotherms obtained at $LN_2$ temperature for the products of the $MoO_3/NH_3$ reaction.

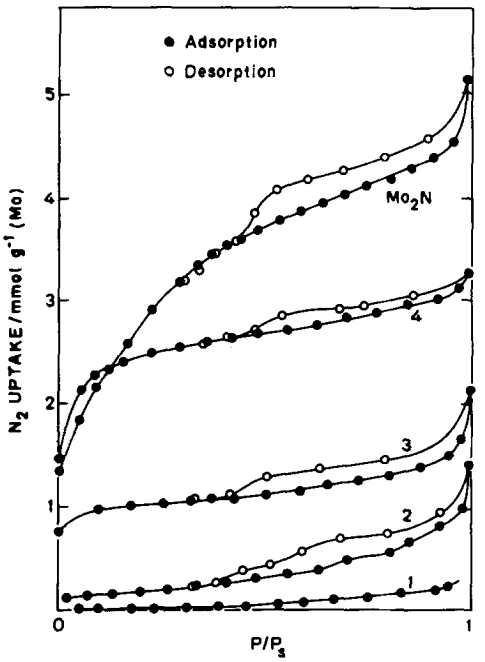


FIG. 11. Equilibrium $N_2$ adsorption and desorption isotherms obtained on the intermediates of the $MoO_3$/$NH_3$ reaction at $LN_2$ temperature. Final reaction temperatures (K): (1) 638, (2) 674, (3) 708, (4) 835, ($Mo_2N$) 980. Table I lists the corresponding $S_g$ values.

From these isotherms, values of $S_g$ were obtained by the standard BET method (Table I). They increased by more than two orders of magnitude in the course of the reaction, reaching 220 $m^2\ g^{-1}$, which represents, as far as we are aware, the highest value on record for unsupported, stable metallic powders. The uptake of $LN_2$ by $Mo_2N$ was 0.15 $cm^3\ g^{-1}$ of Mo (at $P$ = 94 kPa).

The value of $S_g$ = 220 $m^2\ g^{-1}$ was obtained for a fresh sample of $Mo_2N$. Following CO adsorption at RT, it decreased to 190 $m^2\ g^{-1}$. For a passivated $Mo_2N$ sample, $S_g$ = 170 $m^2\ g^{-1}$ and $LN_2$ uptake = 0.123 $cm^3\ g^{-1}$.

The value of $S_g$ for a fresh sample corresponds to an average particle size of ca. 3 nm, calculated as $d_p = 6/\rho S_g$ (*24*), where the density is $\rho$ = 9.5 g $cm^{-3}$ for $Mo_2N$. This value is lower than the estimate for the crystallite size by a factor of 2. Changes in crystal size are common in gas–solid reactions, but the absence of sintering among 3-nm particles in a very reactive environment at 980 K is remarkable.

The isotherms of the reaction intermediates are shaped as a combination of types I and IV (*23*). The type I contribution, characteristic of solids containing pores a few molecular diameters in width, grows with the extent of reaction until at least 825 K, as evidenced by the rise of the nearly horizontal plateau in Fig. 11. For the powders reacted at still higher temperature, the pla-

TABLE I

ADSORPTION DURING THE $MoO_3/NH_3$ REACTION

| Sample[a] | $T^b$ (K) | $S_g^c$ ($m^2\ g^{-1}$) | CO chemisorption[d] ($\mu$mol $g^{-1}$) Total | Irreversible | Ratio of Irreversible to total | $n_{CO}$ ($10^{13}$ $cm^{-2}$) Total | Irreversible |
|---|---|---|---|---|---|---|---|
| $MoO_3$ | 300 | 0.9 | — | — | — | — | — |
| 1 | 638 | 2.3 | $10^{-1}$ | $10^{-1}$ | — | <1 | <1 |
| 2 | 674 | 15 | 5.7 | 1.0 | 0.18 | 2.3 | 0.41 |
| 3 | 708 | 66 | 93 | 45 | 0.48 | 8.5 | 4.1 |
| 4 | 835 | 168 | 900 | 610 | 0.66 | 32 | 21 |
| $Mo_2N$ | 980 | 225 | 1460 | 970 | 0.67 | 39 | 26 |

[a] In accord with Fig. 11.
[b] Final reaction temperature.
[c] Nitrogen BET values referred to 1 g of Mo.
[d] Per 1 g of Mo.

teau becomes steeper due to multilayer adsorption, indicating that the pores increase in width rather than in number. The type IV contribution is manifested in a type B adsorption–desorption hysteresis (*23*). It can be due either to slit-shaped pores or to plate-like particles. Both of these may be present in our samples.

In the process of going from $MoO_3$ to $Mo_2N$, the specific volume (per 1 g of Mo) decreases by 65%. On the other hand, judging from the SEM pictures (Fig. 3), the solid's exterior is retained, although some shrinkage of the platelets cannot be ruled out. At any rate, the material, originally nonporous, developed voids. Its vast internal porosity goes hand in hand with pseudomorphism. Indeed, the uptake of $LN_2$ by $Mo_2N$ corresponds to about 75% of the "lost" volume. The rest is unaccounted for, but some of the pores could be blocked or even be too small for the $N_2$ molecule to penetrate.

The amount of chemisorbed CO at RT (Table I) was found by extrapolating the linear portions of the isotherms to zero pressure. The fraction corresponding to irreversible uptake could not be removed by evacuation at RT. The number density ($n_{CO}$) was calculated as the amount of CO uptake per unit area.

Evidently, the values of $n_{CO}$ corresponding to total and irreversible uptake, as well as the ratio of irreversible to total uptake, increased in the course of the reaction. Molybdenum nitride has $1.1 \times 10^{15}$ surface metal atoms per $cm^2$, an average value corresponding to an equal proportion of the three low-index planes. Thus, about one molecule of CO is chemisorbed irreversibly at RT per four metal atoms at the surface of the final $Mo_2N$ product.

We did not study the changes in $S_g$ and porosity during the $WO_3/NH_3$ reaction. Specific surface area was measured only for the final product. It had the value of 91 $m^2\,g^{-1}$, corresponding to an average particle size of about 4 nm, in good agreement with the estimate of crystallite size. Carbon monoxide chemisorption amounted to 200 $\mu$mol $g^{-1}$.

*Transmission Electron Microscopy*

Unlike the $MoO_3$-JM crystals, some of the $MoO_3$-AM platelets were thin enough to be suitable for TEM. Figure 12 shows a BF image and corresponding SADP of one such platelet. The specimen has contrast features characteristic of variable thickness. The spot pattern belongs to the $[010]_{MoO_3}$ zone axis, which means that the platelet was perpendicular to the electron beam. Since most of the $MoO_3$-AM crystallites lay horizontally on the support, it took very little specimen tilting to achieve this orientation. The strongest reflections (Fig. 12b) are (200) and $(\bar{2}00)$. Along with $h + l$ even spots, less intense $h + l$ odd reflections appear in the pattern due to asymmetrically excited ($h0l$) Laue zones (*21*), just as in the case of the $MoO_3$–VP specimen (Fig. 7b).

Powders of $MoO_3$-AM reacted with $NH_3$ the same way as $MoO_3$-JM, and the final product consisted of pseudomorphous platelets with $S_g = 220$ $m^2\,g^{-1}$ giving only $\gamma$-$Mo_2N$ XRD lines. A BF image and corresponding SADP of a small representative $Mo_2N$ platelet are shown in Fig. 13. In the pattern (Fig. 13b), which is indexed in the Appendix, both the spots and the rings belong to $\gamma$-$Mo_2N$. The reason for the rings is substantial misorientation between the crystallites that comprise the platelet. But the unmistakable square pattern of spots that belongs to the [100] zone axis proves that the $(100)_{Mo_2N}$ planes are predominantly oriented parallel to the platelet—as would be the case with a single crystal—thus confirming the topotactic relationship to $MoO_3$.

The slightly underfocused image (Fig. 13a) shows a random mosaic of small domains on the platelet. This type of image contrast is caused by density variations in

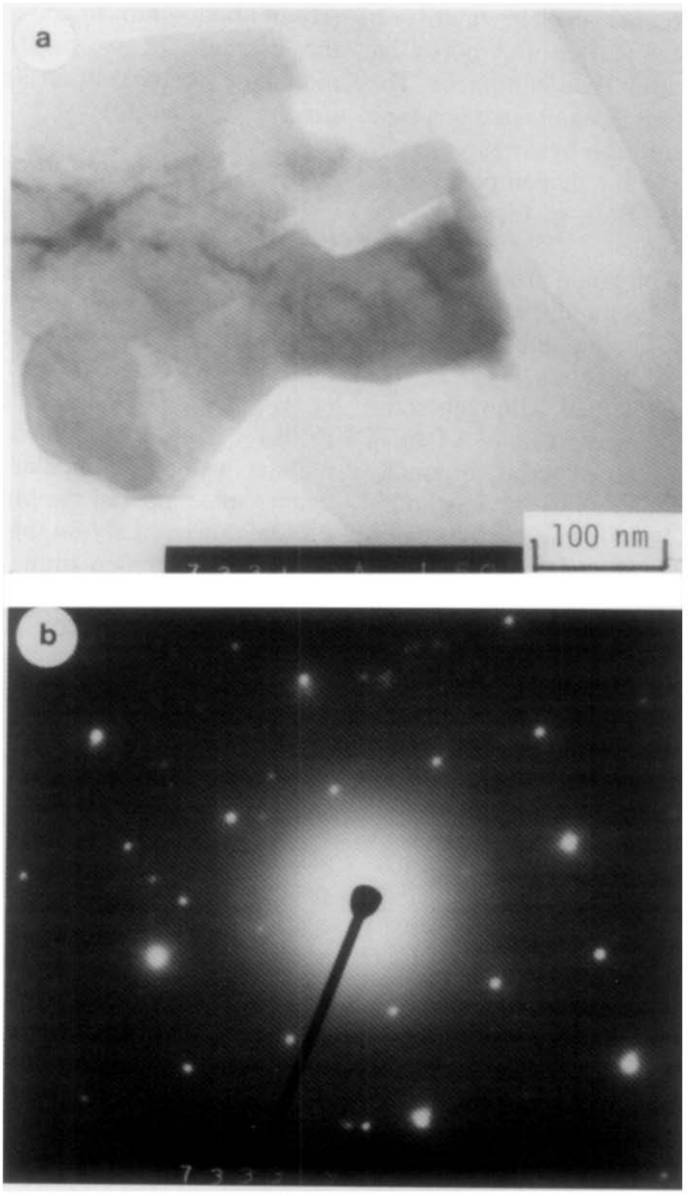


FIG. 12. Transmission electron microscopy of a $MoO_3$-AM platelet. (a) Bright-field image. (b) Corresponding selected-area diffraction pattern belonging to $[010]_{MoO_3}$. The strongest relections are (200) and $(\bar{2}00)$. The $h + l$ odd spots have less intensity.

the specimen and is commonly encountered in porous solids. The mottled image as such, however, does not show a true picture of the platelet's texture because many factors other than its porosity may influence the contrast. Therefore, it would be wrong to draw a direct analogy between the TEM domains and the $Mo_2N$ crystallites, although they are similar in size.

Such a spongy platelet can be viewed as a highly porous defect single crystal of $Mo_2N$. Materials with similar texture and

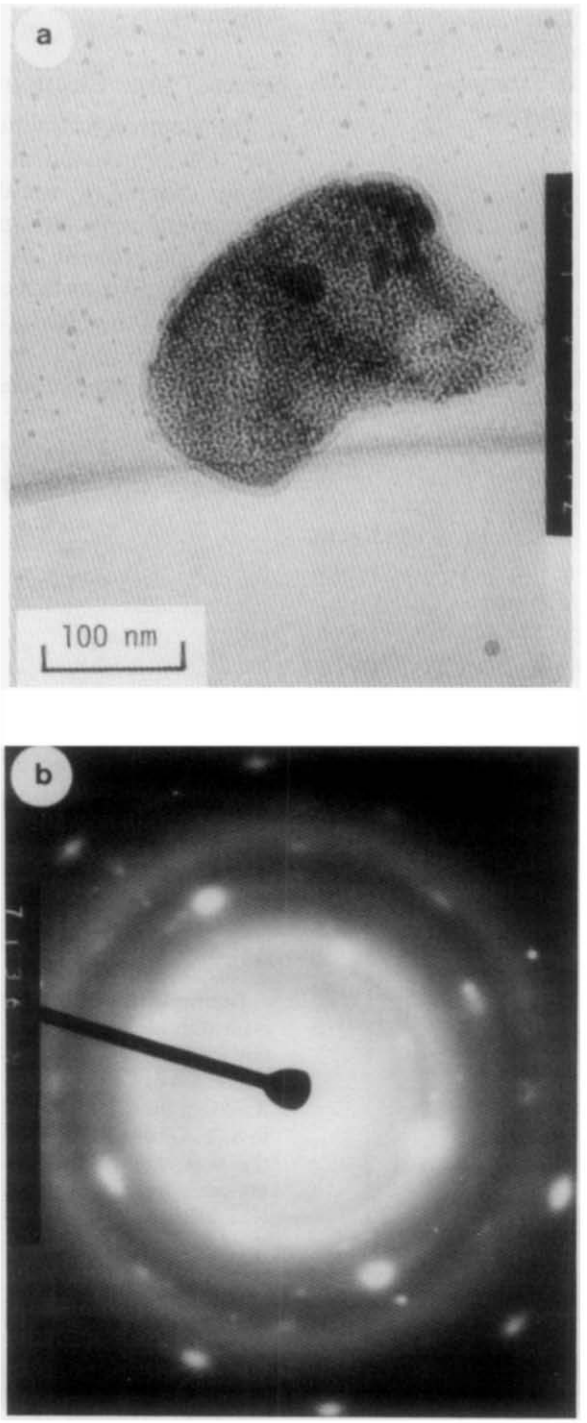


FIG. 13. A small $Mo_2N$ platelet under a transmission electron microscope. (a) Bright-field image (on a carbon-coated TEM grid). (b) The corresponding $Mo_2N$ electron diffraction pattern. The spots show the $\{100\}_{Mo_2N}$ orientation.

structure can be found among some oxides produced by decomposition of hydroxides or salts (*25*). Ours is an example of a metallic solid with such properties.

## Conclusion

Stable $Mo_2N$ and $W_2N$ powders with $S_g$ = 220 and 91 $m^2 g^{-1}$ can be prepared by temperature-programmed reactions between the corresponding trioxides and ammonia. These are the highest values on record for unsupported metallic powders. The nitrides consist of 3- to 4-nm particles aggregated in a spongy relic of the parent trioxide crystals. The $MoO_3/NH_3$ reaction is topotactic because it results in the crystallographic orientation relationship: $\{010\}_{MoO_3}//\{100\}_{Mo_2N}$. The nitride $Mo_2N$ product consists of pseudomorphous platelets that can be regarded as porous single crystals. The average pore size lies below 3 nm. With $WO_3$, an fcc phase is the sole reaction product, but its crystallographic orientation relative to the parent solid is unknown.

Nitride powders with high $S_g$ may be used as such, or after sintering, or as precursors to other materials. Thus, Mo and W carbide powders with high $S_g$ may be obtained from $Mo_2N$ and $W_2N$ by their topotactic reaction in $CH_4$–$H_2$ mixtures (*38*).

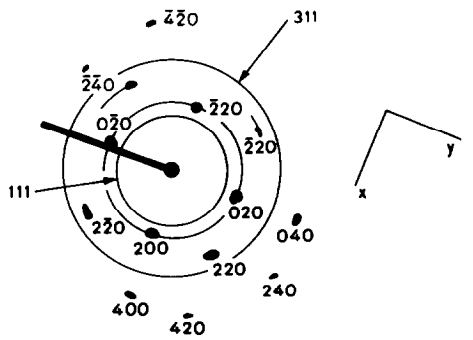


FIG. 14. Indexed electron diffraction pattern of $Mo_2N$, corresponding to Fig. 13b.

## Appendix

### Selected Area Electron Diffraction

The electron diffraction pattern shown in Fig. 13b is indexed in Fig. 14. The interplanar spacing ($d$) is calculated by dividing the camera constant, approximately known for the experiment, by the distance of the spot or ring from the central spot ($r$). The zone axis of the crystal is obtained as a vector product of any two nonequivalent planes whose reflections appear in the pattern.

From Fig. 14, given the camera constant of 400 pm cm, we have for $Mo_2N$:

| | | $d$/pm | |
|---|---|---|---|
| {*hkl*} | *r*/cm | Expt | Ref. (*35*) |
| 111 | 1.6 | 250 | 240 |
| 200 | 1.9 | 210 | 208 |
| 220 | 2.7 | 250 | 247 |
| 311 | 3.1 | 130 | 126 |

Our values of $d$ agree with the reference within experimental error. The zone axis is

$$(200) \times (220) = [002] = [001].$$

## Acknowledgments

Transmission electron microscopy in this study was made possible through the Stanford/NASA Joint Institute for Surface and Microstructure Research. It was performed in collaboration with S. Ichikawa and M. Avalos in the laboratory of H. Poppa. We are grateful to S. T. Oyama for useful discussions. The investigation was initiated with support from the Center for Materials Research at Stanford University under the NSF-MRL Program (NSF-DMR—80-20248-A2).

## References

1. A. A. ANDREEV, L. V. BULATOVA, A. S. BULATOV, G. N., KARTMAZOV, T. V. KOSTRITSA, AND A. A. ROMANOV, *Metalloved. Term. Obrab. Met.* **5**, 33 (1981).
2. A. P. BRODYANSKII, I. A. BUNDA, AND E. A. ANEL'CHISHINA, *Mashinostroitel* **9**, 23 (1977).

3. YU. M. LAKHTIN AND YA. D. KOGAN, *Izv. Akad. Nauk SSSR, Metal.* **5,** 145 (1971).
4. J. R. RAIRDEN, U.S. Patents 3,665,544 and 3,714,013.
5. Z. YOU-XIANG AND H. SHOU-AN, *Solid State Commun.* **45,** 281 (1983).
6. W. E. PICKETT, B. M. KLEIN, AND D. A. PAPACONSTANTOPOULOS, *Physica B + C (Amsterdam)* **107,** 667 (1981).
7. R. B. LEVY AND M. BOUDART, *Science (Washington, D.C.)* **181,** 547 (1973).
8. A. MITTASCH, *in* "Advances in Catalysis and Related Subjects" (W. G. Frankenburg, V. I. Komarewsky, and E. K. Rideal, Eds.), Vol. 2, p. 81, Academic Press, New York (1950).
9. M. SAITO AND R. B. ANDERSON, *J. Catal.* **63,** 438 (1980); **67,** 296 (1977).
10. Y. SHIGEHARA, *Nippon Kagaku Kaishi* **4,** 474 (1977); **10,** 1438 (1977).
11. A. I. KHARLAMOV, *Teor. Eksp. Khim.* **15,** 468 (1979).
12. L. E. TOTH, "Transition Metal Carbides and Nitrides," p. 14, Academic Press, New York (1971).
13. S. T. OYAMA, Ph.D. dissertation. Stanford University (1981).
14. R. KIESSLING AND L. PETERSON, *Acta Metall.* **2,** 675 (1954).
15. M. D. LYUTAYA, *Poroshk. Metall.* **3,** 60 (1978).
16. K. H. CARPENTER AND C. J. HALLADA, *in* "Proceedings, Climax 3rd Intl. Conf. on the Chemistry and Uses of Molybdenum" (H. F. Barry and P. C. H. Mitchell, Eds.), p. 204, Climax Molybdenum Company, Ann Arbor (1979).
17. T. FRANSEN, P. C. VAN BERGE, AND P. MARS, *React. Kinet. Catal. Lett.* **5,** 445 (1976).
18. F. V. HANSON, Ph.D. dissertation. Stanford University (1975).
19. S. F. BERTRAM, *in* "Handbook of X-Rays" (E. F. Kaelble, Ed.), Chap. 17, McGraw-Hill, New York (1967).
20. B. WANKLYN, *J. Cryst. Growth* **2,** 251 (1968).
21. L. A. BURSILL, *Proc. R. Soc. London Ser. A* **311,** 267 (1969).
22. G. ANDERSSON AND A. MAGNÉLI, *Acta. Chem. Scand.* **4,** 793 (1950).
23. J. H. DE BOER, *in* "The Structure and Properties of Porous Materials" (D. H. Everett and F. S. Stone, Eds.), pp. 68–94, Butterworth, London (1958).
24. S. J. GREGG AND K. S. W. SING, "Adsorption, Surface Area and Porosity," pp. 30–36, Academic Press, New York/London (1982).
25. L. VOLPE AND M. BOUDART, *Catal. Rev.-Sci. Eng.* **27,** 515 (1985).
26. W. F. MCCLUNE, Ed., "Powder Diffraction File, Inorganic Compounds," JCPOS, pattern 5-0508, Swarthmore (1980).
27. G. ANDERSSON, *Acta Chem. Scand.* **7,** 154 (1953).
28. J. A. PERRY, E. BANKS, AND B. POST, *J. Appl. Phys.* **28,** 1272 (1957).
29. O. GLEMSER AND G. LUTZ, *Kolloid Z.* **119,** 99 (1950).
30. H. KÖNIG, *Z. Phys.* **130,** 483 (1951).
31. H. HASHIMOTO, *J. Phys. Soc. Jpn.* **9,** 150 (1954).
32. E. PERNOUX AND R. BORRELLI, *J. Microsc.* **2,** 407 (1963).
33. P. L. GAI, *Philos. Mag.* **43,** 841 (1981).
34. L. KIHLBORG, *Adv. Chem. Ser.* **39,** 37 (1981).
35. W. F. MCCLUNE, Ed., "Powder Diffraction File, Inorganic Compounds," JCPOS, pattern 25-1366, Swarthmore (1980).
36. H. R. OSWALD AND J. R. GÜNTER, *in* "1976 Crystal Growth and Materials" (E. Kaldis and H. J. Scheel, Eds.), p. 415, North Holland, Amsterdam (1977).
37. O. BERTRAND AND L. C. DUFOUR, *Phys. Status Solidi A* **60,** 507 (1980).
38. L. VOLPE AND M. BOUDART, *J. Solid State Chem.* **59,** 348 (1985).